DERIVING SURFACE TEMPERATURE OF NAAMEH LANDFILL AND ITS SURROUNDINGS USING LANDSAT 8 OLI AND TIRS ACQUISITIONS

Elie El Khoury[1], Charbel Abou Khalil[2], and Elsy Ibrahim*
Department of Civil and Environmental Engineering, Notre Dame University – Louaize, Lebanon
[1]Email: ejkhoury01@ndu.edu.lb
[2]Email: cjaboukhalil01@ndu.edu.lb
*Corresponding author: eibrahim@ndu.edu.lb

KEYWORDS: Atmospheric Correction, Emissivity, Thermal Infrared

ABSTRACT: Thermal remote sensing can be very helpful for landfill monitoring since biogas generation leads to an increase in temperature during the aerobic and anaerobic digestion processes. The objective of this study is to derive the land surface temperature (L_S) of Naameh Landfill – located in Lebanon – and its surroundings in different seasons using Landsat 8 (L8) acquisitions. As such, two L8 images were acquired to analyze the characteristics of this landfill. The images were corrected using four algorithms of which three are split window algorithms and one is single channel technique. The study found that the L_S variation between the landfill and its surroundings can be successfully obtained through different correction methods presented in this paper. However, L_S was found to be changing for the same class when applying the different algorithms where the inconsistency ranged from 0.4 ºK to 4 ºK. ANOVA tests showed statistically significant difference in means of all methods. As for the variation in L_S between the landfill and different classes, it was found to be consistent for three techniques. This difference was lowest between the landfill and bare soils (maximum of 3 ºK in summer). On the other hand, the maximum difference from the Ls of the landfill was with the sea in summer (~12.5 ± 1.5ºK). However, Ls of the landfill did not vary greatly from its surroundings during winter, and thus necessitating the use of TRS during summer when monitoring Landfills due to their significant microbial activity at higher temperatures. Finally, the impact of ϵ on L_S derivation using each method was assessed.

1. INTRODUCTION

Satellite thermal remote sensing (TRS) is becoming increasingly popular during the last three decades since it allows the retrieval of the land surface temperature (L_S). The latter is one of the most essential physical parameters of surface energy since it is used in environmental monitoring (Su, 2002; Voogt & Oke, 2003) like the monitoring of landfills by analyzing soil, water, and produced landfill gas (Spokas et al., 2006; Faisal et al., 2012). When only in-situ monitoring is used, it requires tremendous efforts and cost since landfills have a large spatial footprint. Thus, cheap, quick, and non-destructive methods of monitoring are becoming popular. TRS is one of those approaches because landfills have significantly higher L_S when compared to their surroundings. Due to anaerobic biological degradation of organic waste inside the landfill, biogas which contains methane (~ 60%) is generated and has the ability to absorb the sun's heat and to increase the landfill's L_S (Spokas et al., 2006; Faisal et al., 2012). This makes landfills a significant source of energy. However, methane is also a highly potent greenhouse gas (25 times that of CO_2 (IPCC, 2007)). As such, monitoring methane generation is a must, and since it is linked to L_S, great potential exists with the use of TRS. However, in order to obtain L_S, TRS images should undergo corrections to account for the effects of the atmosphere and emissivity (ϵ), where ignoring such adjustments would lead to an error ranging from 1 to 5 ºK (Dash et al., 2002; Prata et al., 1995; Jiménez-Muñoz et al., 2014). Also, the error due to improper ϵ estimation for different land covers is not well investigated and what is simply known is that the error in L_S increases as ϵ decreases (Sharma et al., 2017).

In 2013, Landsat 8 (L8) satellite was launched and includes Operational Land Imager (OLI) multispectral sensor of nine channels and Thermal Infrared sensor (TIRS) of two bands (Roy et al., 2014) that acquires images with a spatial resolution of 100 m (Du et.al, 2015). The presence of two thermal bands allows the application of simple and robust atmospheric correction methods like split-window algorithms (SWAs) (Jiménez-Muñoz et al., 2014; Rozenstein et al., 2014; Du et al., 2015; Yu et al., 2014) that benefit from differential absorption between the spectrally discrete bands (Band 10: 10.60 – 11.19 µm; Band 11: 11.50 – 12.51 µm) in order to account for (1) water-vapor absorption (ω) in the atmosphere and (2) the proportionality between the atmospheric absorption of the radiant signal and the radiance difference of the two thermal bands, where each band is attenuated differently by the atmosphere (Jiménez-Muñoz & Sobrino, 2003; Yu et al., 2014). However, single channel algorithms (SC) for atmospheric correction are more accurate (Dash et al., 2002) but time consuming and require atmospheric data which can be unavailable (Jiménez-Muñoz et al., 2014). For every algorithm, be it for SWA or SC, adjustment for ϵ varies and requires careful consideration (Jiménez-Muñoz et al., 2014; Rozenstein et al., 2014; Du et al., 2015; Yu et al., 2014; Sharma et al., 2017). This study investigates the variation of L_S retrieved from L8 when applying several atmospheric

correction methods, namely one SC and three SWA developed for TIRS, and while considering ϵ. Moreover, the study investigates L_S variation between the landfill and its surroundings during the wet and cold winter and the dry and hot summer seasons.

2. STUDY AREA

Naameh landfill (Fig. 1), located in Chouf district – Lebanon, is considered to be the most important sanitary disposal site in Lebanon since it was receiving waste from greater Beirut area and Mount Lebanon, equivalent to 58% of the total national waste generation (Massoud et al., 2010). It has significantly vegetated surroundings with mostly evergreen species (Arif & Doumani, 2014).

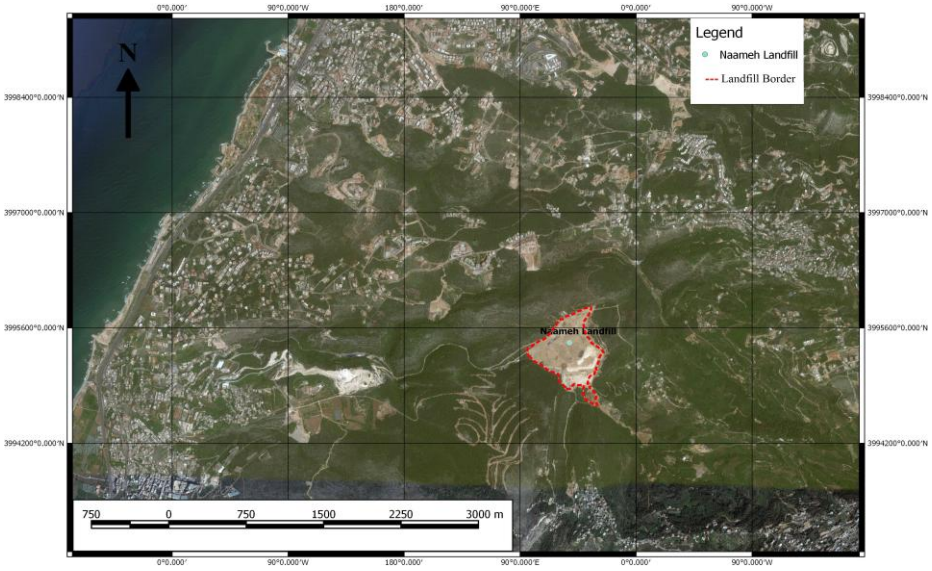

Figure 1: Naameh landfill (delineated in red) and its surrounding, image taken from Google Earth on July 2017

Naameh landfill started in 1997 and was planned to serve for six years. Yet, it received waste for 18 years (till summer 2015). Its last reported area in 2014 was about 350,000 m^2 (Arif & Doumani, 2014; Zakhem et al., 2016). Residents of Naameh town and its surroundings have been protesting since 2000 that it is loaded far beyond ability and can be a source of health and environmental risks (MOE/UNDP/ECODIT, 2011). By 2014, the waste dumped in this landfill reached 12 million tons which is larger than the design capacity by four folds (Arif & Doumani, 2014). After closure, a waste crisis occurred in Lebanon and forced the government to reopen the landfill for a short emergency period. Regarding the biogas emitted from the anaerobic degradation in the subsurface, it was being flared during the entire period of the landfill's operation. Lately, however, the biogas was used to supply the locals in Naameh with electricity. The landfill would generate biogas several years after closure and thus be able to yield a significant amount of energy.

3. MATERIALS & METHODS

3.1 Overview

The workflow described in the following sections is shown in Fig. 2.

3.2 Data acquisition, preprocessing, and classification

Two L8 images were acquired from the United States Geological Survey (USGS) for winter and summer (Table 1). Following the workflow diagram, the OLI images were classified after determining reflectance values and applying dark object subtraction (DOS) to correct for the atmospheric effects successively (Dash et al., 2002). Support vector machine (SVM) supervised classification was done using the ENVI-IDL^{TM} environment using training data acquired from Google Earth and site visits. Six classes resulted, namely Landfill, Bare Soil, Mixed (Vegetation & Soil), Heavy Vegetation, Urban areas, and Sea (Fig. 3). Data from the TIRS was also corrected to transform the digital numbers to at-sensor temperature (T_{sen}) (Fig. 4) by reversing the Planck's function (Dash et.al, 2002).

Table 1: L8 Images Characteristics used in this study

Season	Acquisition Date (Month/Day/Year)	Time (UTC)	Path/ Row	Satellite	Ambient Temperature (ºK)
Winter	02/13/14	8:09 AM	174/37	L8	291.5
Summer	06/08/15	8:10 AM	174/37	L8	300.0

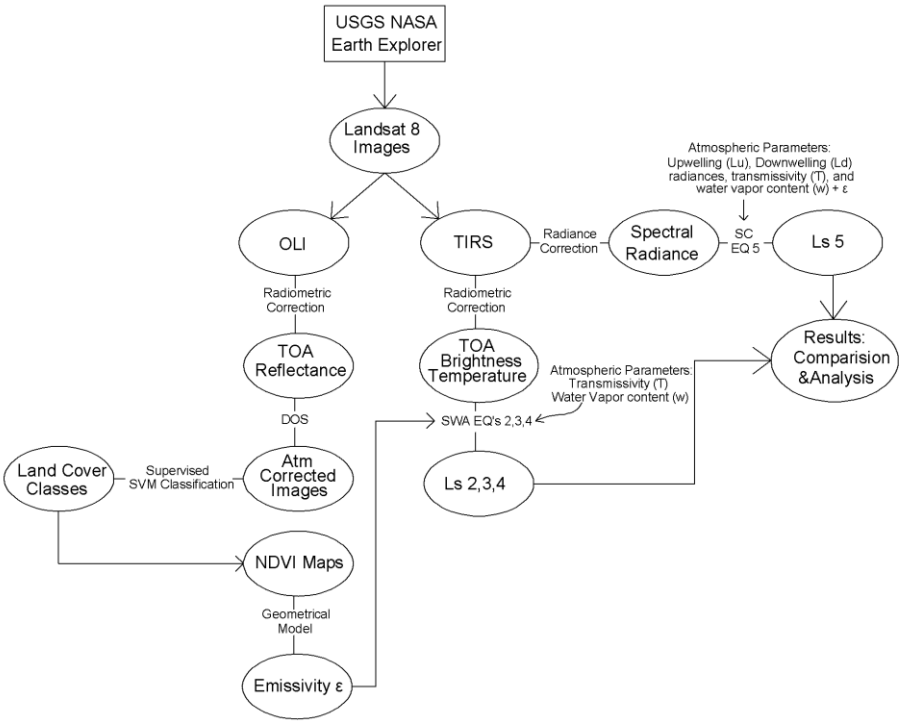

Figure 2: Workflow Diagram

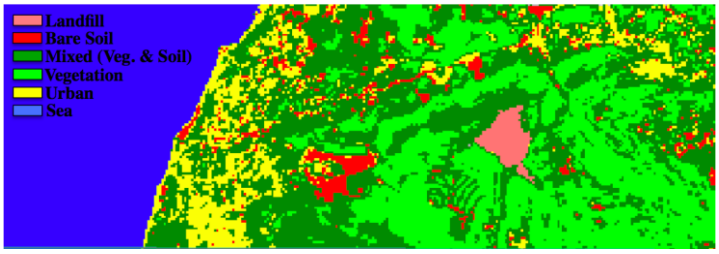

Figure 3: Classification of the study area using SVM (based on the summer image)

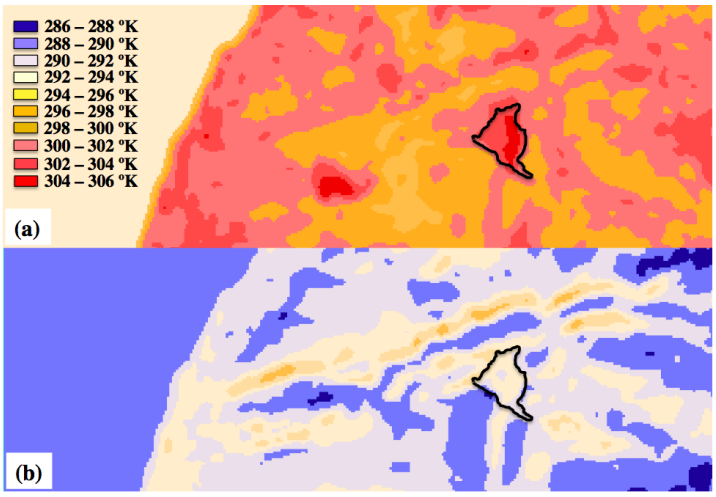

Figure 4: T_{sen} maps determined from L8 TIRS acquisitions of (a) summer and (b) winter

3.3 Estimating Emissivity

The normalized difference vegetation index (NDVI) was determined for the images. ϵ for each pixel was determined using EQ. 1 developed by Van de Griend & Owe (1993). Fig. 5 shows ϵ in summer and provides the average ϵ per class. However, it should be noted that EQ. 1 is not valid when having a negative NDVI such as the case of water (NDVI ~ -0.4). Thus, water ϵ was considered constant for all pixels (= 0.989) (Valor & Caselles, 1996). The ϵ variation between the two images was also very low (maximum of 0.5%) which is due to the fact that the NDVI variation between images was minimal. Furthermore, ϵ is considered constant for both L8 TIR bands even though it is wavelength dependent since the variation in the 8 to 14 μm range is minimal (Hori et al, 2006 & Jensen, 2009).

$$\epsilon = 1.0094 + 0.047 ln(NDVI) \quad \textbf{(1)}$$

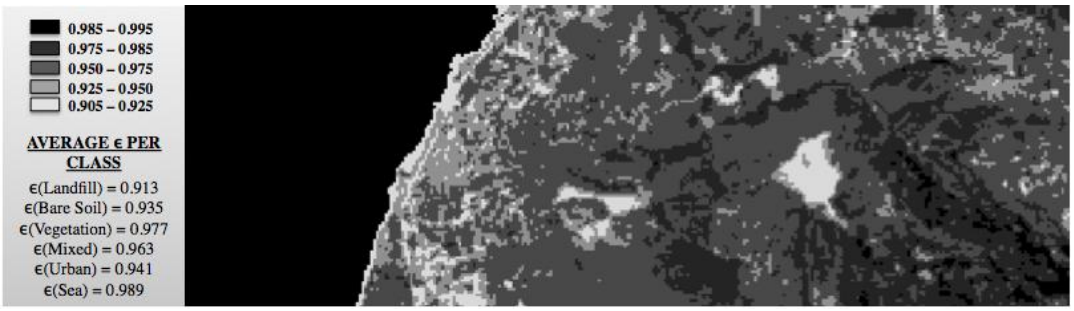

Figure 5: ϵ map for the study area

3.4 Deriving L_S from T_{sen}

For deriving the L_S from T_{sen}, three SWA and one SC algorithms specific to L8 were used. The first SWA adopted in this study is presented in EQ. 2 and was derived by Du et al. (2015). It includes the addition of the last quadratic term (difference between adjacent T_{sen}) which was derived after 946 atmospheric conditions retrieved from Thermodynamic Initial Guess Retrieval (http://ara.abct.lmd.polytechnique.fr) and 53 ϵ spectra from ASTER database. The algorithm coefficients are also specific to L8 TIRS and depend on different ranges of ɯ.

$$L_s = b_o + (b_1 + b_2(1-\epsilon)/\epsilon + b_3 \Delta\epsilon/\epsilon^2) * 0.5(T_{10}+T_{11}) + (b_4 + b_5(1-\epsilon)/\epsilon + b_6 \Delta\epsilon/\epsilon^2) * 0.5(T_{10}-T_{11}) + b_7(T_{10}-T_{11})^2 \quad \textbf{(2)}$$

where $[b_0, b_1 \ldots, b_7]$ = [11.00824, 0.95995, 0.17343,-0.28852, 7.41192, 0.42684, -6.62925, -0.06381] for a ɯ ranging between 2 and 3.5 g/cm^2 and $[b_0, b_1 \ldots, b_7]$ = [-2.78009, , 1.01408, 0.15833, -0.34911, 4.04487, 3.55414, -8.88394, 0.09152] for a ɯ ranging between 0 and 2.5 g/cm^2. T_{10} and T_{11} are the T_{sen} for bands 10 and 11, respectively.

The second SWA, presented in EQ. 3 was developed by Yu et al. (2014) by adopting the same mathematical derivation suggested by Quin et al. (2001). For EQ. 3, transmissivity (Ƭ) is estimated by quadratic regression analysis versus ɯ. This algorithm also requires the estimation of ɯ and ϵ.

$$L_s = T_{10} + c_1*(T_{10} - T_{11}) + c_0 \quad \textbf{(3)}$$

where c_o and c_1 are linear regression coefficients in function of Ƭ and ϵ.

The third SWA was developed by Rozenstein et al. (2014) and is presented in EQ. 4 derived through algebraic manipulation of the radiative transfer equation and linearization of the Planck's radiance equation. The algorithm requires the estimation of ϵ and Ƭ.

$$L_s = a_o + a_1 T_{10} - a_2 T_{11} \quad \textbf{(4)}$$

where a_o, a_1, and a_2 are linear regression coefficients in function of Ƭ and ϵ.

The fourth and final algorithm adopted in this study is presented in EQ. 5 and was developed by Jimenez-Muñoz et al. (2014). EQ. 5 is a SC algorithm derived by the inversion of the radiative transfer equation (Jiménez-Muñoz & Sobrino, 2003). The algorithm requires the estimation of ϵ, T, upwelling radiance (L_u), and downwelling radiance (L_d).

$$L_s = \gamma * [1/\varepsilon (d_1 * L_{sen} + d_2) + d_3] + \delta \quad (5)$$

where L_{sen} is the at sensor spectral radiance in $W.m^{-2}.sr^{-1}.\mu m^{-1}$ calculated from the two TIRS images; γ and δ are parameters represented by $\gamma = T_{sen} / b_\gamma.L_{sen}$, $\gamma = T_{sen} - T_{sen}^2 / b_\gamma$, and $b_\gamma = c_2/\lambda = 1324$ for TIRS band 10; d_1, d_2, and d_3 are atmospheric functions where $d_1 = 1/\tau$, $d_2 = L_d - L_u/\tau$, and $d_3 = L_d$. However, if τ, L_d, and L_u are not available, Jiménez-Muñoz et al. (2014) provides an approximation of d_1, d_2, and d_3 by plotting them against ω from a second order polynomial fit. In this study, τ, L_d, and L_u were determined by the software developed by Barsi et al. (2003).

4. RESULTS & DISCUSSION

4.1 Variation of retrieved L_S with Different Atmospheric correction algorithms

L_S maps for each class and for both summer and winter images are provided in Fig. 6 and 7, respectively. The difference between T_{sen} and L_s ranges from 1 to 8ºK for all the correction methods and hence is higher than what has been recorded in literature (1 to 5 ºK). The one-way analysis of variance (ANOVA) (Tamhane, 1977) test is used to compare the means of the obtained Ls images and to determine whether at least two means of two groups are statistically different, meaning it tells us if there is an overall difference of means. To investigate specifically which of the means are different from each other, a post-hoc test should be conducted. Due to its great presence in the images, the sea water was masked out of both scenes, and all ANOVA analysis was carried out with the land pixels.

For the ANOVA test, one should check the following assumptions for the groups (Clarke, 2008): (1) each should follow a normal distribution; (2) they should have homogenous variances. Table 2 summarizes statistical characteristics of each of the L_s maps obtained by EQ. 2, EQ. 3, EQ. 4, and EQ. 5. Normality is considered a valid assumption based on histogram plots of summer data show in Fig. 8. However, for the winter data (Fig. 8), normality is attained only when the logarithm is applied and therefore the data follows a log-normal distribution. For variance homogeneity assessment, a box and whisker plot is in Fig. 9 to visualize the spread, skewness, and outliers in the data. Since all the boxes are of roughly the same height, then this shows that the groups have approximately equal variance.

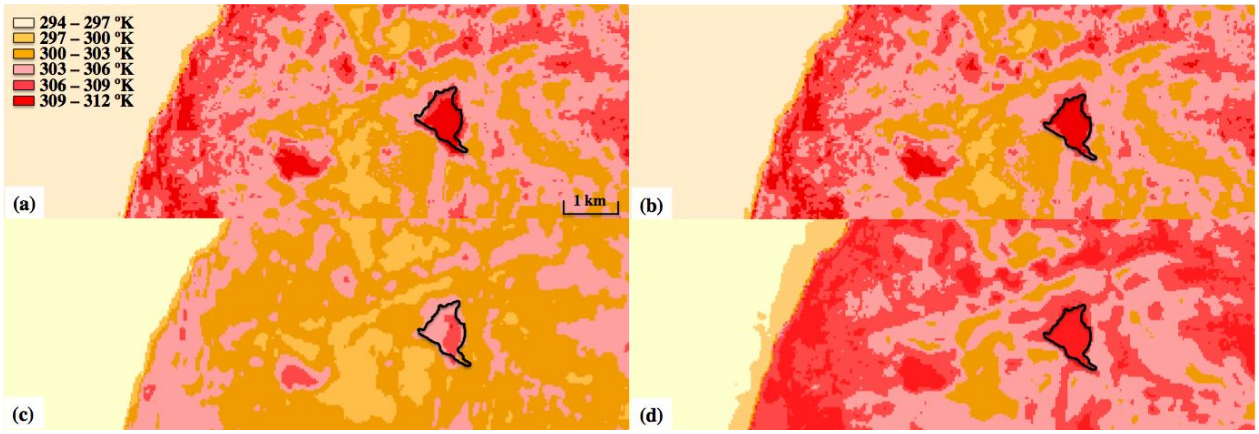

Figure 6: L_S maps for the summer image when applying (a) EQ. 2, (b) EQ. 3, (c) EQ. 4, and (d) EQ. 5

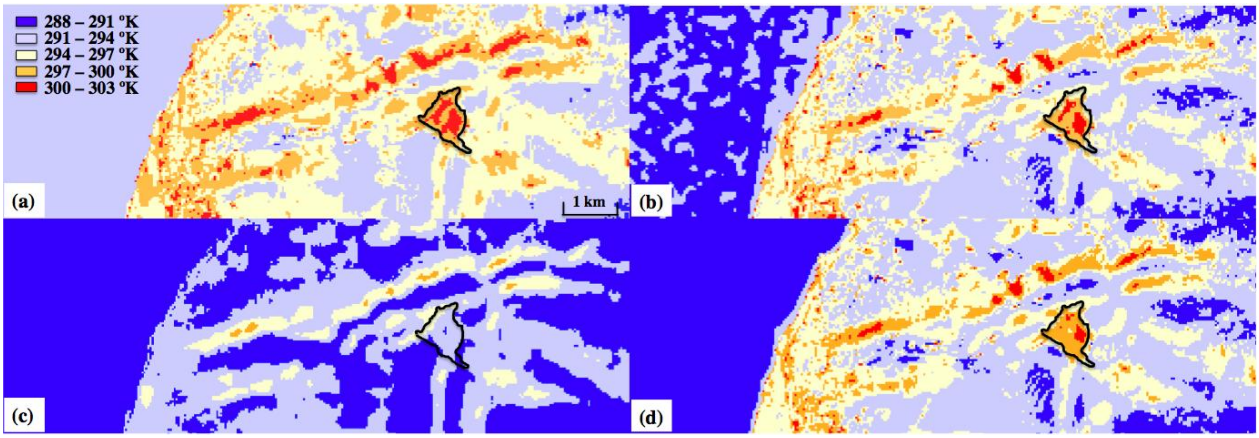

Figure 7: L_S maps for the winter image when applying (a) EQ. 2, (b) EQ. 3, (c) EQ. 4, and (d) EQ. 5

ANOVA is applied on the four different L_S achieved by the four methods as a whole, per season. It resulted that there was a statistically significant difference between their means as determined by one-way ANOVA [F (df) = F ratio, p] = [F (3) = 24937, $p\text{-value} < 2\times10^{-16}$]; where F is the F statistic, df is the degrees of freedom and p is the p-value. Since the p-value is very small and less than the assumed alpha value of 0.05, then the one-way ANOVA null hypothesis is wrong and there is an overall statistically significant difference in means. ANOVA residual plots show the normality of residuals, and thus assert the validity of ANOVA for this dataset (Fig. 10). To determine how the pair means are statistically different from each other, the post hoc "Tukey Honest Significant Differences" multiple comparison test is used. The test does a pair-wise comparison of the means of L_S and reports the p-value shown Table 3. The four different L_S maps are compared to each other in Fig. 11 and since in each case the p-value is less than the alpha confidence value of 0.05, then a significant statistical difference is seen in the group's means. It can be noted that the most similar results were obtained for EQ. 2 and EQ. 3 (b-a), yet the highest difference in the results is between EQ. 4 and EQ. 5 (c-d). The single channel algorithm (EQ. 5) seems to be mostly consistent with EQ. 3 (b-d).

Table 2: Description of summer and winter data groups

Summer				
Group	**Mean**	**Std. Deviation**	**Minimum**	**Maximum**
a	304.640	2.656	297.009	319.570
b	304.713	2.578	297.250	314.972
c	302.277	1.873	296.553	309.049
d	306.640	2.611	298.707	314.991

Winter				
Group	**Mean**	**Std. Deviation**	**Minimum**	**Maximum**
a	295.841	2.115	289.600	304.200
b	294.054	2.376	288.500	304.680
c	292.137	1.901	279.343	299.950
d	294.671	2.216	288.287	308.200

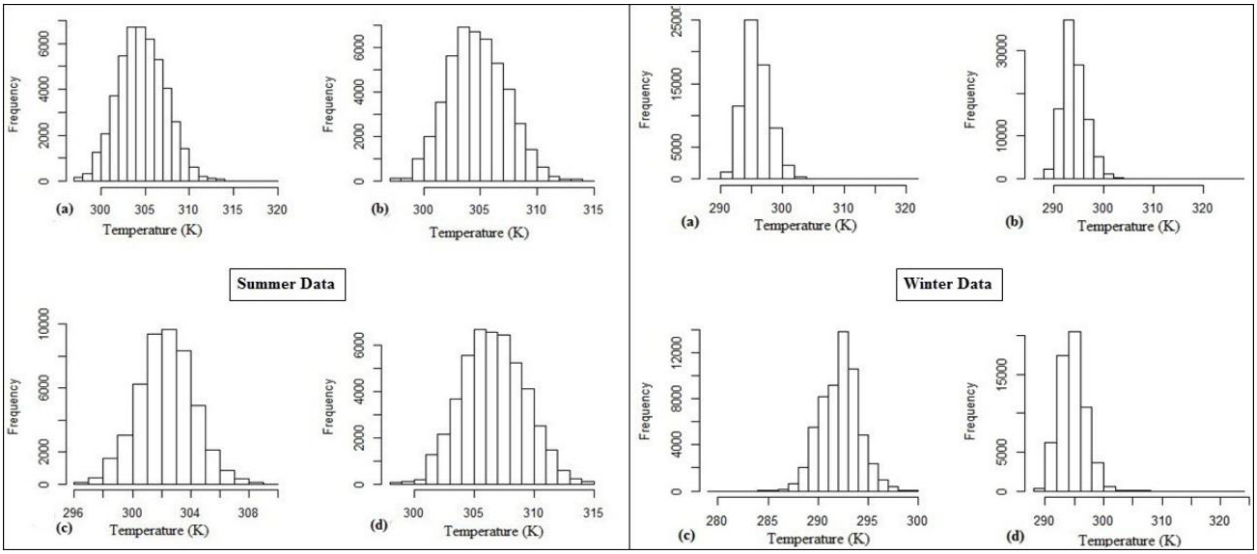

Figure 8: Histogram plot of Frequency vs. Temperature when applying (a) EQ. 2, (b) EQ. 3, (c) EQ. 4, and (d) EQ. 5 for both summer and winter maps (excluding sea water)

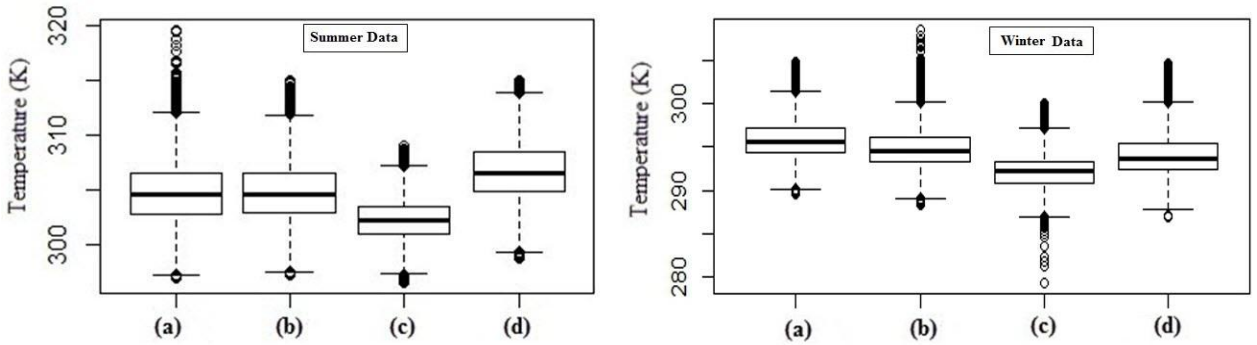

Figure 9: Box and Whisker plots for the four different groups for the summer and winter data (excluding sea water)

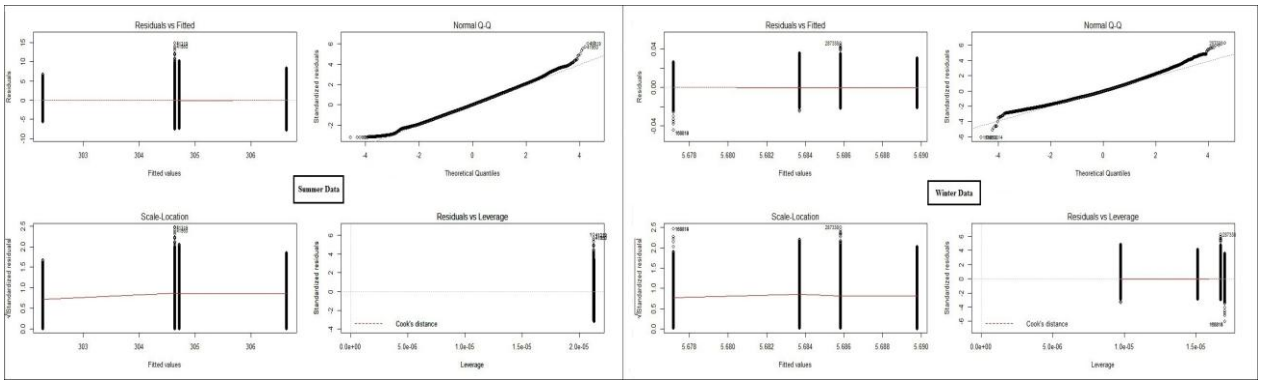

Figure 10: ANOVA residual plots for both summer and log-transformed winter (excluding sea water) data respectively on the left and right

Table 3: Tukey multiple comparisons of means with 95% family-wise confidence level

Summer					
Group (I)	Group (J)	Mean Difference (I-J)	Significane p-value	95% Confidence	
				Lower Bound	Upper Bound
d	a	2.0000	~0	1.9589	2.0410
c	a	-2.3637	~0	-2.4048	-2.3226
b	a	0.0728	0.0000313	0.0317	0.1139
c	d	-4.3636	~0	-4.4047	-4.3226
b	d	-1.9272	~0	-1.9683	-1.8861
b	c	2.4365	~0	2.3954	2.4776

Winter						
Group (I)	Group (J)	Mean Difference (I-J) (log-transformed)	Mean Difference (I-J) (original values)	Significane p-value	95% Confidence	
					Lower Bound	Upper Bound
d	a	-0.00396	-1.1740	~0	-0.00407	-0.00386
c	a	-0.01259	-3.7130	~0	-0.01270	-0.01249
b	a	-0.00610	-1.7960	~0	-0.00619	-0.00600
c	d	-0.00863	-2.5390	~0	-0.00874	-0.00852
b	d	-0.00213	-0.6220	~0	-0.00223	-0.00203
b	c	0.00650	1.9170	~0	0.00640	0.00660

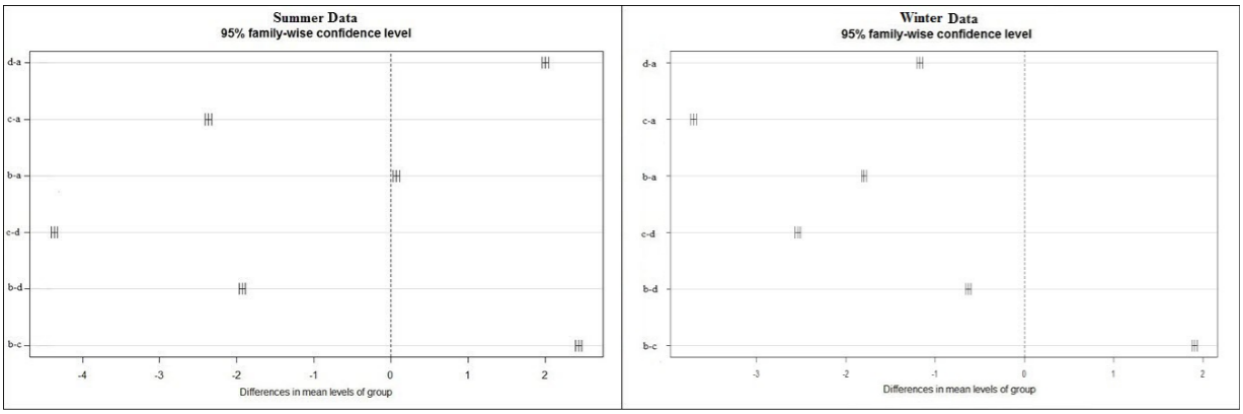

Figure 11: Tukey Multiple Comparison Test. All groups' means are compared to each other and the difference is reported on the x-axis, the further the plot is from the zero dotted vertical lines the higher is the statistically significant difference, a is EQ. 2, b is EQ. 3, c is EQ. 4, and d is EQ. 5 (data excludes sea water)

4.2 Variation of the L_S between the landfill and the surrounding

Fig. 12 displays the L_S difference between the landfill and the surroundings for both images for each of the four atmospheric correction methods. The difference is relatively high, especially during summer, which confirms the ability of this thermal data in capturing the activeness of the landfill at higher temperature. For both winter and summer images, the smallest difference is encountered when applying EQ. 4 while EQ. 2, 3 and 5 give higher differences and are consistent with each other. In addition, the difference in Ls between the landfill and the vegetation is about 2 to 7 ^oK during the summer and hence is consistent with the literature (Faisal et al., 2012). On the whole, the variation in L_S between different classes was found, during summer, to be minimal (~1.7 ± 0.3 ^oK) between the landfill and bare soils and maximum (~12.5 ± 1.5^oK) between landfill and the sea temperature.

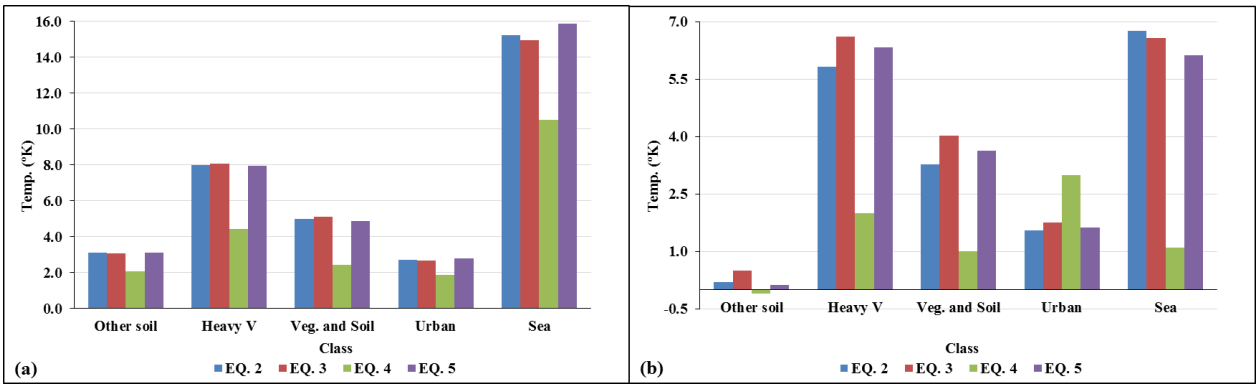

Figure 12: L_S difference between the landfill and the other classes for the (a) summer image, and (b) winter image

4.3 Effect of the ϵ on the difference between T_{sen} and L_S (ΔT)

ϵ has a great impact on determining L_S from TIR images, and it can be noticed that in each of the correction equations, it plays a role. However, different atmospheric correction algorithms might impact L_S results depending on how ϵ is accounted for. Fig. 13 provides T_{sen} - Ls (ΔT) when accounting for ϵ for the different atmospheric correction algorithms for both summer and winter images. As shown in Fig. 13, ΔT varies from 0.2 to 6 °K for an ϵ ranging from 0.913 to 0.989 for both images when applying EQ. 2, 3 and 5. However, for EQ. 4, which represent the algorithm developed by Rozenstein et al. (2014), the difference is much smaller (0.03 to 1.5 °K) which highlights the reason why the L_S obtained from this correction algorithm is much smaller than the other correction procedures and hence needs to be investigated further. Since EQ. 2, 3 and 5 - when considering ϵ - are yielding consistent results, a linear correlation can be derived between ΔT and ϵ, as shown in Fig. 14(b), with an R^2= 0.9925.

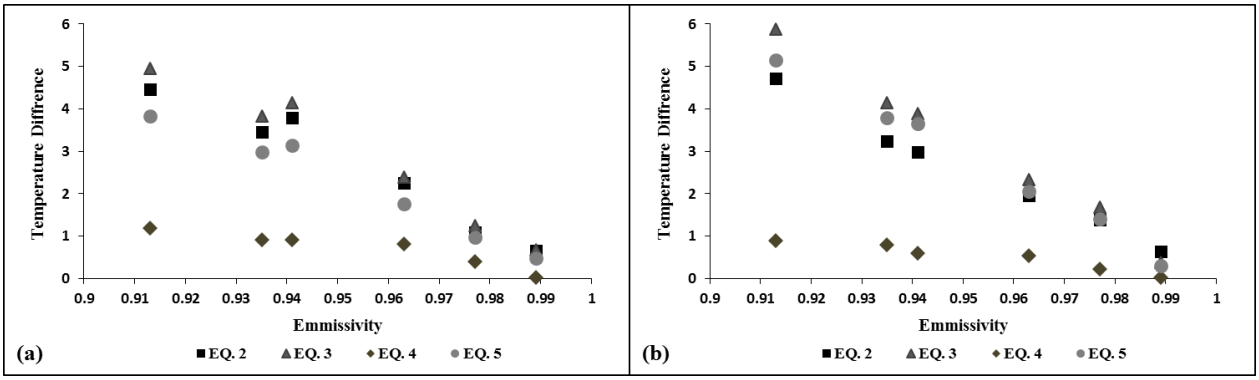

Figure 13: Average ΔT in °K for with correction methods w.r.t. ϵ for (a) summer and (b) winter

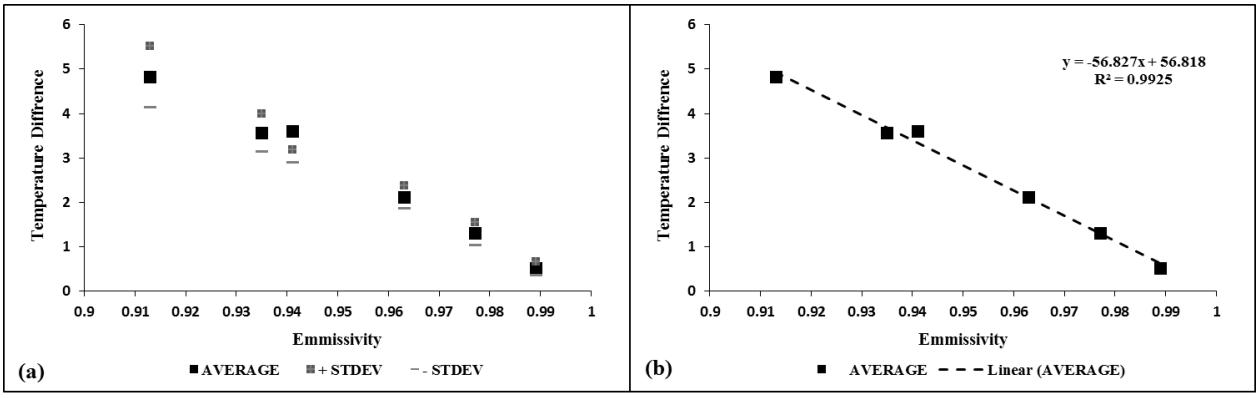

Figure 14: (a) ΔT in °K between the T_{sen} and L_S with respect to ϵ for EQ. 2, 3 and 5; (b) linear correlation between ϵ and ΔT

5. CONCLUSION

L8 data was used to obtain thermal information of Naameh Landfill which can be linked to the different anaerobic microbiological phases. The study found that L_S variation between the landfill and its surroundings can be successfully obtained in a consistent manner through two different approaches of SWA (out of three tested) and the one SC algorithm presented in this paper. This confirms the success in using these techniques quantify the relative difference in temperature per scene. Yet, the absolute temperature results per methods were inconsistent with variation ranging from 0.4 ^oK to 4 ^oK. Hence, L_S determined from all the algorithms cannot be validated unless compared to the actual L_S which is the upcoming step in this work. In addition, the variation in L_S between different classes was found, during summer, to be minimal (~1.7 ± 0.3 ^oK) between the landfill and bare soils and maximum (~12.5 ± 1.5^oK) between landfill and the sea temperature. However, minor changes of the L_S between the landfill and the surrounding was observed during winter, and thus necessitating the use of TRS during summer when monitoring Landfills due to their significant microbial activity at higher temperatures. On the whole, this study shows the effectiveness of the four different approaches in the retrieval of the relative variation in Ls in the summer and winter. Furthermore, a study was conducted to analyze the effect of ϵ variation on the temperature difference between T_{sen} and Ls (ΔT), it was found that a linear correlation exists between the ϵ and the ΔT (for adopting the different correction algorithms) with an R^2 of 0.9925. Finally, to confirm the statistical significance of the four different corrections in summer and winter, the ANOVA test was conducted. Along with the post hoc Tukey test, ANOVA resulted that the several adopted approaches indeed show a statistical significant difference among their means in general and in pairwise comparison.

REFERENCES

Arif, S., & Doumani, F., 2014. Lebanon, Cost Assessment of Solid Waste Degradation in Beirut and Mount Lebanon. GiZ SWEEP-Net, Tech. Rep.

Barsi, J. A., Barker, J. L., & Schott, J. R., 2003. An atmospheric correction parameter calculator for a single thermal band earth-sensing instrument. In Geoscience and Remote Sensing Symposium, 2003. IGARSS'03 Proceedings 2003 IEEE International, Vol. 5, pp. 3014-3016.

Change, I. C., 2007. Mitigation of climate change. Summary for Policymakers, 10(5.4).

Clarke, B. R., 2008. Linear models: the theory and application of analysis of variance (Vol. 634). John Wiley & Sons.

Dash, P., Göttsche, F. M., Olesen, F. S., & Fischer, H., 2002. Land surface temperature and emissivity estimation from passive sensor data: theory and practice-current trends. International Journal of remote sensing, 23(13), pp. 2563-2594.

Du, C., Ren, H., Qin, Q., Meng, J., &Zhao, S., 2015. A practical split-window algorithm for estimating land surface temperature from Landsat 8 data. Remote Sensing, 7(1), pp. 647-665.

Faisal, K., AlAhmad, M., & Shaker, A., 2012. Remote sensing techniques as a tool for environmental monitoring. International Archives of the Photogrammetry, Remote Sensing and Spatial Information Sciences, pp. 39-43.

Hori, M., Aoki, T., Tanikawa, T., Motoyoshi, H., Hachikubo, A., Sugiura, K, & Takahashi, F. (2006). In-situ measured spectral directional emissivity of snow and ice in the 8–14 μm atmospheric window. Remote Sensing of Environment, 100(4), 486-502.

Jensen, J. R., 2009. Remote sensing of the environment: An earth resource perspective 2/e. Pearson Education India.
Jiménez-Muñoz, J. C., & Sobrino, J. A., 2003. A generalized single-channel method for retrieving land surface temperature from remote sensing data. Journal of Geophysical Research: Atmospheres, 108(D22).

Jiménez-Muñoz, J. C., Sobrino, J. A., Skoković, D., Mattar, C., & Cristóbal, J., 2014. Land surface temperature retrieval methods from Landsat-8 thermal infrared sensor data. IEEE Geoscience and Remote Sensing Letters, 11(10), pp. 1840-1843.

Massoud, M. A., Fayad, R., El-Fadel, M., & Kamleh, R., 2010. Drivers, barriers and incentives to implementing environmental management systems in the food industry: A case of Lebanon. Journal of Cleaner Production, 18(3), pp. 200-209.

MOE/UNDP/ECODIT, “State of the Environment Report,” Ministry of Environemnt, Tech. Rep., 2011. From http://www.moe.gov.lb/The-Ministry/Reports/State-Of-the-Environment-Report-2010.aspx?lang=en-us.

Prata, A. J., Caselles, V., Coll, C., Sobrino, J. A., & Ottle, C., 1995. Thermal remote sensing of land surface temperature from satellites: Current status and future prospects. Remote Sensing Reviews, 12(3-4), pp. 175-224.

Quin, Z., Dall’Olmo, G., Karnieli, A., & Berluser, P., 2001. Derivation of split window algorithm and its sensivity analysis for retrieving land surface temperature from NOAA-AVHRR data. J. Geophys. Res, 106(D19), pp. 22655-22670.

Roy, D.P., Wulder, M.A., Loveland, T.R., Woodcock,C.E., Allen, R. G., Anderson, M. C., ... & Scambos, T. A., 2014. Landsat-8: Science and product vision for terrestrial global change research. Remote Sensing of Environment, 145, pp. 154-172.

Rozenstein, O., Qin, Z., Derimian, Y., & Karnieli, A., 2014. Derivation of land surface temperature for Landsat-8 TIRS using a split window algorithm. Sensors, 14(4), pp. 5768-5780.

Sharma, A. K., Sharma, S. K., Vasistha, P., & Mangalhara, J. P., 2017. Estimation of Effect of Emissivity on Target Detection through Thermal Imaging Systems. Defence Science Journal, 67(2), pp. 177.

Spokas, K., Bogner, J., Chanton, J. P., Morcet, M., Aran, C., Graff, C, & Hebe, I., 2006. Methane mass balance at three landfill sites: What is the efficiency of capture by gas collection systems?. Waste management, 26(5), pp. 516-525.

Su, Z., 2002. The Surface Energy Balance System (SEBS) for estimation of turbulent heat fluxes. Hydrology and Earth System Sciences Discussions, 6(1), pp. 85-100.

Tamhane, A. C., 1977. Multiple comparisons in model I one-way ANOVA with unequal variances. Communications in Statistics-Theory and Methods, 6(1), 15-32.

Valor, E., & Caselles, V., 1996. Mapping land surface emissivity from NDVI: Application to European, African, and South American areas. Remote sensing of Environment, 57(3), pp. 167-184.

Van de Griend, A. A., & Owe, M., 1993. On the relationship between thermal emissivity and the normalized difference vegetation index for natural surfaces. International Journal of remote sensing, 14(6), pp. 1119-1131.

Voogt, J. A., & Oke, T. R., 2003. Thermal remote sensing of urban climates. Remote sensing of environment, 86(3), pp. 370-384.

Yu, X., Guo, X., &Wu, Z., 2014. Land surface temperature retrieval from Landsat 8 TIRS - Comparison between radiative transfer equation-based method, split window algorithm and single channel method. Remote Sensing, 6(10), pp. 9829-9852.